

# Diquark properties from full QCD lattice simulations

A. Francis<sup>a</sup>, Ph. de Forcrand<sup>b</sup>, R. Lewis<sup>c</sup> and K. Maltman<sup>d,e</sup>

<sup>a</sup>Albert Einstein Center, CH-3012 Bern, Switzerland,

<sup>b</sup>CERN, CH-1211 Geneva, Switzerland,

<sup>c</sup>Department of Physics and Astronomy, York University, Toronto, Ontario, M3J 1P3, Canada,

<sup>d</sup>Department of Mathematics and Statistics, York University, Toronto, Ontario M3J 1P3, Canada,

<sup>e</sup>CSSM, University of Adelaide, Adelaide, SA, 5005, Australia

(Dated: June 18, 2021)

We study diquarks on the lattice in the background of a static quark, in a gauge-invariant formalism with quark masses down to almost physical  $m_\pi$ . We determine mass differences between diquark channels as well as diquark-quark mass differences. The lightest and next-to-lightest diquarks have “good” scalar,  $\bar{3}_F, \bar{3}_c, J^P = 0^+$ , and “bad” axial vector,  $6_F, \bar{3}_c, J^P = 1^+$ , quantum numbers, and a bad-good mass difference for  $ud$  flavors, 198(4) MeV, in excellent agreement with phenomenological determinations. Quark-quark attraction is found only in the “good” diquark channel. We extract a corresponding diquark size of  $\sim 0.6$  fm and perform a first exploration of the “good” diquark shape, which is shown to be spherical. Our results provide quantitative support for modeling the low-lying baryon spectrum using good light diquark effective degrees of freedom.

*Introduction.*— Diquarks are old [1–3], but have been enjoying renewed popularity, see *e.g.* [4–6], making a detailed, ab initio study on the lattice useful and timely.

Diquarks are made up of two quarks and consequently carry an open color index. Thus, like quarks, they do not exist as asymptotic states. Since contracting a diquark with a quark produces a baryon operator, a diquark with an anti-diquark a tetraquark operator, *etc.*, effective diquark degrees of freedom may be useful building blocks for phenomenological descriptions of hadronic states. The success of such a description would depend on diquarks being compact objects with fewer degrees of freedom than the quark pairs they stand for. The phenomenological success of diquark models [6–9] supports this possibility, provided one assumes the diquarks have “good diquark” ( $\bar{3}_F, \bar{3}_c, J^P = 0^+$ ) flavor, color and Dirac quantum numbers. This assumption is natural given that one-gluon-exchange [10, 11] and instanton interactions [12–14] are both attractive in this channel. The present work aims to investigate this picture quantitatively via results on diquark masses and sizes/spatial correlations from first-principle simulations of QCD on the lattice. Since diquarks are colored, and not gauge-invariant, neither are their properties. To deal with this, one can, *e.g.*, work in a fixed gauge, typically Landau gauge or a variant thereof, see, *e.g.*, the lattice studies of Refs. [15–17]. The drawback is that the resulting diquark masses and sizes depend on the gauge choice. This is a well-known problem for the size determination [18–20], though diquark masses, and even mass differences, are affected as well since these are extracted from the temporal decay rates of appropriate correlators, which will change in a gauge which is non-local in time like Landau gauge. Alternately, one can introduce a static color source which, together with the diquark, forms a color singlet baryon, whose mass is gauge-invariant. Since the mass of such a static-light-light baryon diverges in the continuum limit, the quantities of interest are mass *dif-*

*ferences* between various diquark channels. The diquark size can also be obtained in a gauge-invariant way, from the spatial decay rate of the quark density-density correlator at a fixed time [21–26]. This size might, in principle, depend on the diquark-static source separation, though we find no evidence for such dependence.

We adopt the second, gauge-invariant approach. Measurements are taken on dynamical  $n_f = 2 + 1$ ,  $32^3 \times 64$ , clover-improved Wilson fermion gauge configurations with lattice spacing  $a \approx 0.090$  fm [27, 28] generated by the PACS-CS collaboration [27, 28] and publicly available from the JLDG repository [29]. Five ensembles, with pion masses  $\{164, 299, 415, 575, 707\}$  MeV are studied, allowing us to observe, for the first time, the dependence of diquark properties on the light, dynamical quark mass, and perform a small, controlled extrapolation to physical  $m_\pi$ . We re-use the quark propagators from [30, 31]. To connect with previous quenched studies, we also perform measurements on a new  $32^3 \times 64$ ,  $a \approx 0.092$  fm, quenched ensemble with a valence pion mass  $m_\pi = 909$  MeV. Static quark propagators are computed using the method of [32, 33] with HYP1 smearing. See Appendix II for further details.

*Diquark spectroscopy.*— We first quantify the expected reduction in the “good” diquark mass by studying the static-light-light baryon spectrum. With  $Q$  the static quark, and light quarks in a  $D_\Gamma = q^c C \Gamma q$  diquark configuration, where  $c, C$  denote charge conjugation, and  $\Gamma$  acts in Dirac space, we measure the baryon correlators

$$C_\Gamma(t) = \sum_{\vec{x}} \langle [D_\Gamma Q](\vec{x}, t) [D_\Gamma Q]^\dagger(\vec{0}, 0) \rangle. \quad (1)$$

$\Gamma = \gamma_5, \gamma_5 \gamma_0$  for “good”,  $0^+$  diquarks,  $\gamma_i$  for “bad”,  $1^+$  diquarks, and  $\mathbf{1}$  and  $\gamma_5 \gamma_i$ , for the “not-even-bad”, odd-parity  $0^-$  and  $1^-$  diquarks. We also measure the correlators of the static-light meson operators  $[\bar{Q} \Gamma q]$ . The static quark ( $m_Q \rightarrow \infty$ ) acts as a spectator; its mass cancels in mass differences, exposing the diquark spectrum.

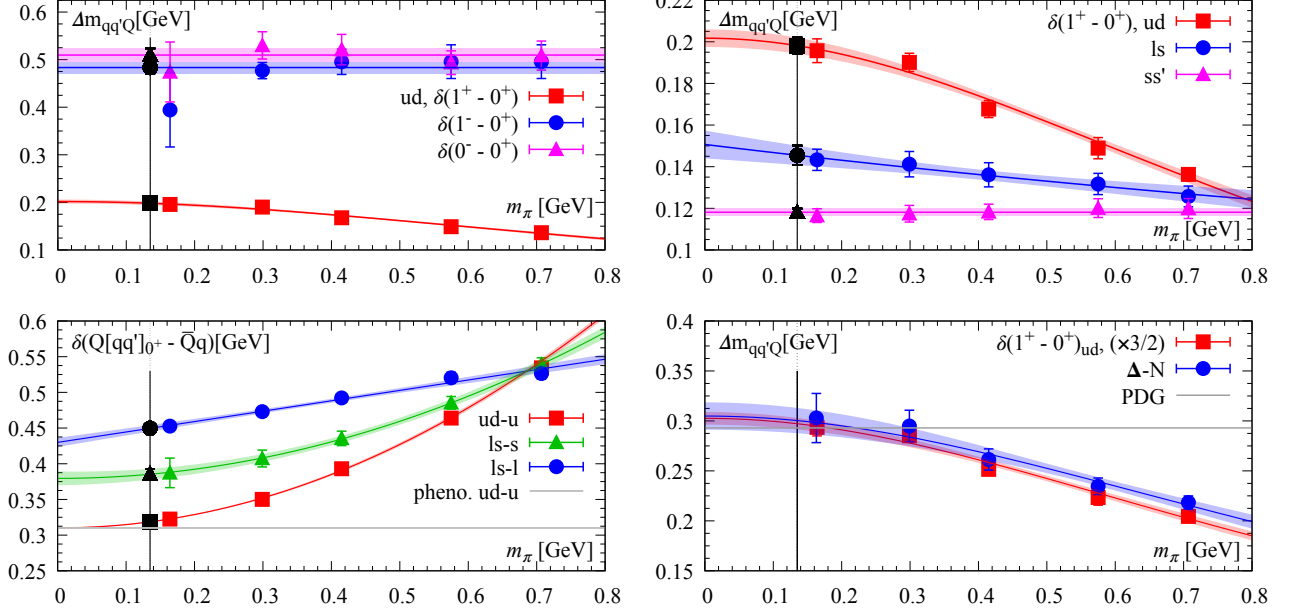


FIG. 1. *Diquark spectroscopy: mass differences as a function of  $m_\pi$ . Vertical lines identify physical  $m_\pi$ . (Top left) The  $ud$  diquark mass differences  $\delta(1^+ - 0^+)$ ,  $\delta(1^- - 0^+)$  and  $\delta(0^- - 0^+)$ . (Top right) Bad-good  $ud$ ,  $ls$  and  $ss'$  diquark mass differences, with extrapolations to the physical-point using the Ansatz Eq. (2). (Bottom left) Analogous  $Qqq - \bar{Q}q$  mass differences, extrapolated using Eq. (3). The horizontal line is the phenomenological value  $\delta(b[ud]_{0^+} - \bar{b}u) = 310$  MeV [4]. (Bottom right) Agreement of the bad-good diquark mass splitting with the prediction [4],  $\delta(\Delta - N) = 3/2 \times \delta(1^+ - 0^+)_{ud}$ .*

We consider diquarks with light-light ( $ud$ ), light-strange ( $ls$ ), and strange-strange' ( $ss'$ ) flavors.  $s'$  denotes a hypothetical additional strange valence quark, introduced to allow a study of the mass of a good diquark composed of two quarks, each with the strange quark mass, which the flavor antisymmetry of the good diquark configuration makes inaccessible to two identical  $s$  quarks. Our analysis is repeated on our 5 ensembles, with different light quark, and hence pion, masses. Technical aspects of the analysis are summarized in App. III.

Figure 1 (top left panel) shows the dependence of the ( $ud$ )  $0^+$ ,  $1^+$ ,  $0^-$  and  $1^-$  diquark mass differences on  $m_\pi$ . The results provide quantitative support for the phenomenological diquark approach, in which only good  $0^+$  diquarks are considered. Explicitly, the good  $0^+$   $ud$  diquark lies lowest in the spectrum, 100-200 MeV below the bad  $1^+$   $ud$  diquark. The negative-parity  $0^-$  and  $1^-$   $ud$  diquarks lie even higher,  $\sim 0.5$  GeV above the good diquark and will thus play no role in the low-energy physics. The same pattern is observed in the  $ls$  and  $ss'$  sectors. Figure 1 (top right panel) compares the  $ud$ ,  $ls$  and  $ss'$  ( $1^+ - 0^+$ ) splittings. The curves in Fig. 1 correspond to fits using Ansätze guided by limiting cases. Explicitly, the ( $1^+ - 0^+$ ) mass difference goes to a constant in the chiral limit and decreases as  $1/(m_{q_1}m_{q_2})$ , with  $m_\pi \sim (m_{q_1} + m_{q_2})$ , in the heavy-quark limit. The simplest interpolation between these two limits is the two-parameter form

$$\delta(1^+ - 0^+)_{q_1q_2} = A / [1 + (m_\pi/B)^n], \quad (2)$$

with  $n = 0, 1, 2$  for  $q_1q_2 = ss'$ ,  $ls$  and  $ud$ , respectively. The parameter  $A$  fixes the chiral limit behavior, while  $B$  separates the light- and heavy-quark regimes. The fits clearly describe the data very well. In [22], a similar ansatz was proposed, but with  $n$  twice as large and a much poorer fit. Note that the  $ud$ ,  $ls$  and  $ss'$  curves in the top right panel all intersect at the flavor-symmetric  $n_f = 3$  point,  $m_{u,d} \rightarrow m_s$ . The parameter values and physical-point mass differences are listed in the top half of Table I. As detailed in App. I, the latter are in excellent agreement with phenomenological expectations [4].

Further information on the diquark spectrum is provided by the mass splittings between static  $Qqq'$  baryons and the corresponding static  $\bar{Q}q$  or  $\bar{Q}q'$  mesons. Results for the  $Qud - \bar{Q}u$ ,  $Qls - \bar{Q}l$  and  $Qls - \bar{Q}s$  combinations are shown in the bottom left panel of Fig. 1, together with fits to an Ansatz similar to Eq. (2),

$$\delta(Q[q_1q_2]_{0^+} - \bar{Q}q_2) = C [1 + (m_\pi/D)^n]. \quad (3)$$

Here,  $C$  fixes the value in the chiral limit, and  $D$  separates the light- and heavy- $q_1$  quark regimes. In the latter, the mass splitting must grow linearly with the mass of  $q_1$ , which dictates  $n = 2$  if  $q_1$  is a light quark,  $n = 1$  otherwise. The fit parameter values and resulting extrapolated physical-point mass differences are listed in the bottom half of Tab. I.

Finally, we can compare the bad-good diquark mass difference with the  $\Delta - N$  mass splitting by measuring the latter for each of our 5 ensembles. In the one-gluon-exchange approximation, and chiral limit, Ref. [4] obtains

All in [GeV]	$\delta E(m_\pi^{\text{phys}})$	A	B
$\delta(1^+ - 0^+)_{ud}$	0.198(4)	0.202(4)	1.00(5)
$\delta(1^+ - 0^+)_{\ell s}$	0.145(5)	0.151(7)	3.7(15)
$\delta(1^+ - 0^+)_{ss'}$	0.118(2)	0.118(2)	
		C	D
$\delta(Q[ud]_{0^+} - \bar{Q}u)$	0.319(1)	0.310(1)	0.814(8)
$\delta(Q[\ell s]_{0^+} - \bar{Q}s)$	0.385(9)	0.379(10)	1.09(6)
$\delta(Q[\ell s]_{0^+} - \bar{Q}\ell)$	0.450(6)	0.430(6)	2.95(35)

TABLE I. Fit parameters  $A, B, C, D$  and physical-point bad-good diquark (top half) and good diquark-quark (bottom half) mass differences, with statistical errors only.

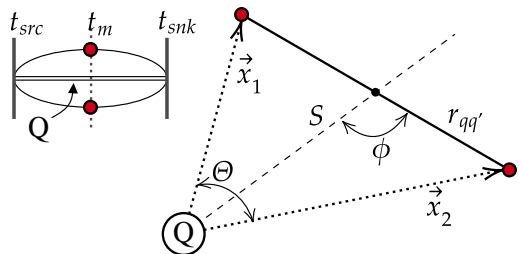


FIG. 2. Pictorial representation of the density correlators. (Top inset) 2D temporal view. The currents are inserted at  $t_m = (t_{\text{snk}} + t_{\text{src}})/2$  and all light propagators use gauge-fixed wall sources. (Main) Sketch of the current insertions used to study diquark attraction and determine the good diquark spatial profile.

$\delta(\Delta - N) = \frac{3}{2}\delta(1^+ - 0^+)$ . The bottom right panel of Fig. 1 compares the left- and right-hand sides of this relation, the red curve showing the appropriately rescaled version of the  $\delta(1^+ - 0^+)_{ud}$  fit of the top right panel and the blue curve a similar fit to the  $\Delta - N$  data with  $A = \frac{3}{2} \times 0.203(9)$ ,  $B = 1.10(11)$  GeV. Agreement between the two is excellent in the chiral limit, and remains very good over the whole mass range.

*Diquark structure.*— Next we compute quark density-density correlators of the form:

$$C_\Gamma^{dd}(\vec{x}_1, \vec{x}_2, t) = \left\langle \mathcal{O}_\Gamma(\vec{0}, 2t) \rho(\vec{x}_1, t) \rho(\vec{x}_2, t) \mathcal{O}_\Gamma^\dagger(\vec{0}, 0) \right\rangle \quad (4)$$

where  $\rho(\vec{x}, t) = \bar{q}(\vec{x}, t) \gamma_0 q(\vec{x}, t)$  and  $\mathcal{O}_\Gamma$  are the baryon operators used before. The label  $\Gamma$  characterizes the diquark channel. With the static quark at the origin, the light-quark source and sink points are  $(\vec{0}, t_{\text{src}})$  and  $(\vec{0}, t_{\text{snk}})$ . The currents are inserted at  $t_m = (t_{\text{snk}} + t_{\text{src}})/2$  which maximises ground-state saturation. The relative positions of the static source and current insertions  $\vec{x}_1, \vec{x}_2$ , can be characterized using  $r_{qq'} = |\vec{x}_2 - \vec{x}_1|$ , the separation,  $S$ , between the static source and midpoint between  $\vec{x}_1$  and  $\vec{x}_2$ , and  $\phi$ , the angle between  $\vec{x}_2 - \vec{x}_1$  and the line from the static source to this midpoint, as shown in Fig. 2. We then define

$$\rho_2(r_{qq'}, S, \phi; \Gamma) \equiv C_\Gamma^{dd}(\vec{x}_1, \vec{x}_2, t_m), \quad (5)$$

dropping the label  $\Gamma$  whenever this produces no confusion.

For fixed  $S$  and  $r_{qq'}$ , the distance from the static source to the closer of the two insertion points is minimized for  $\phi = \pi$  and maximized for  $\phi = \pi/2$ . If the proximity of a static source disrupts the diquark correlation in a given channel, this disruption will thus be largest for  $\phi = \pi$  and smallest for  $\phi = \pi/2$ . We therefore focus our attention on  $\rho_2$  for these two cases. When  $\phi = \pi/2$ ,  $|\vec{x}_1| = |\vec{x}_2| \equiv R$ , and we may instead characterize the relative positions using  $R$  and the angle  $\Theta$  between  $\vec{x}_1$  and  $\vec{x}_2$ . We define  $\rho_2^\perp(R, \theta) \equiv \rho_2(r_{qq'}, S, \pi/2)$  and  $\rho_2^\parallel(r_{qq'}, S) \equiv \rho_2(r_{qq'}, S, \pi)$ . In our calculation we average over all spatial translations.

The impact of the light-quark interactions on the spatial correlation between light quarks in the various diquark channels is displayed in the top panel of Fig. 3, which shows the density-density correlations  $\rho_2^\perp(R, \Theta, \Gamma)$  as a function of  $\cos(\Theta)$ . For illustration, we show the results for all  $\Gamma$  at  $R = 4.1a$  for the ensemble with  $m_\pi = 575$  MeV. The light quark separation decreases from  $2R$  to zero as  $\cos(\Theta)$  increases from  $-1$  to  $+1$ . The clear increase in  $\rho_2$  seen in the good diquark channel is absent in all other channels [34]. The strengths of the quark-quark attractions in the good and bad diquark channels are quantified in the bottom panel of Fig. 3, which shows the  $m_\pi$  dependence of the ratios  $\rho_2^\perp(R, \Theta = 0, \Gamma) / \rho_2^\perp(R, \Theta = \pi/2, \Gamma = \gamma_5)$  for  $\Gamma = \gamma_5$  and  $\gamma_i$ . The ratio is 2 or more for the good diquark across the whole range of  $m_\pi$ , but consistent with 0 for the bad diquark. There is no evidence, within errors, that the ratio varies with decreasing  $m_\pi$ , though there might be an enhancement at low  $m_\pi$  for the good diquark. In any case, we confirm a significant attractive quark-quark spatial correlation in the good diquark channel not present in the bad diquark channel, for the  $m_\pi$ 's studied here.

With a significant attractive good diquark spatial correlation established, we can refine our picture of the good diquark by studying its size and shape. We consider first the case  $\phi = \pi/2$ . At fixed  $R$ ,  $\rho_2^\perp(R, \Theta, \Gamma = \gamma_5)$  depends only on  $\Theta$  or, equivalently,  $r_{qq'} = R\sqrt{2(1 - \cos(\Theta))}$ . We find that this dependence is well represented by an exponential form,  $\rho_2^\perp(R, r_{qq'}) \sim \exp(-r_{qq'}/r_0)$ , for each value of  $R$ . As  $R$  decreases and the diquark moves closer to the static quark, one might expect the static quark to distort such diquark correlations and cause  $r_0$  to vary. We see no evidence for such a variation, so long as  $R > r_{qq'}$ , and thus, in the top panel of Fig. 4, display results for all  $R$  together, for each  $m_\pi$ . We take  $r_0$  as our definition of the good diquark size and fix its value from a combined fit to data for all such  $R$ . The resulting  $r_0(m_\pi^2)$  are displayed, and compared to those obtained in Refs. [22, 24], in the bottom panel of Fig. 4. Recall that our quenched results are derived from a simulation that matches exactly the parameters of [22]. Our results are in very good agreement with [22], and with both the quenched and dynamical results of [24].

As  $m_\pi$  increases, one might expect the heavier quarks to form a more compact object. The results for the  $1^+ - 0^+$  diquark splittings in Tab. I, however, show a weakening of

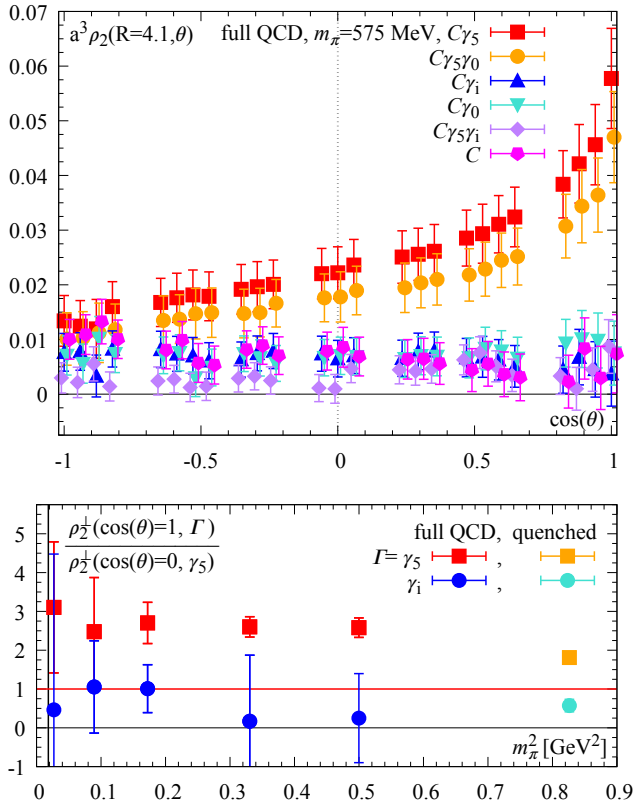


FIG. 3. Diquark attractive effect. (Top) The density-density correlators  $\rho_2^\perp(R = 4.1a, \Theta, \Gamma)$  versus  $\cos(\Theta)$  at  $m_\pi = 575$  MeV. (Bottom) The ratio  $\rho_2^\perp(R, \Theta = 0, \Gamma) / \rho_2^\perp(R, \Theta = \pi/2, \Gamma = \gamma_5)$  versus  $m_\pi^2$ . Values above/below 1 for the red/blue points signal an attraction in the good diquark that is absent for the bad diquark. The vertical line denotes physical  $m_\pi$ .

the good-diquark attraction with increasing quark mass, which one expects to work in the opposite direction. We see some evidence that the former effect dominates for larger  $m_\pi$  (above  $\sim 400$  MeV) though, in the limit of infinitely massive sea quarks (*i.e.* the quenched case) the diquarks are definitely larger. As Fig. 4 indicates, in full QCD, over a range of  $m_\pi$ ,  $r_0$  is of the order of 0.6 fm, a size similar to that of static-light mesons when measured the same way [35]. It may thus be useful to allow for a non-zero diquark size when constructing diquark models of the baryon spectrum.

Finally, we can learn about the good diquark shape, by comparing the density-density correlation falloff for the radial ( $\phi = \pi$ ) and tangential ( $\phi = \pi/2$ ) orientations of the diquark separation to the line from the diquark midpoint to the static source (see Fig. 5). We define separate *radial* ( $\parallel$ ) and *tangential* ( $\perp$ ) size parameters,  $r_0^\parallel$  and  $r_0^\perp$ , from exponential fits to the data for  $\rho_2^\perp(R, \Theta)$  and  $\rho_2^\parallel(r_{qq'}, S)$ , detailed in App. IV and shown in the top panels of Fig. 6.

The ratio  $r_0^\perp / r_0^\parallel$  provides a measure of whether the diquarks are prolate, oblate, or neither. The results are shown in the bottom panel of Fig. 6. We find

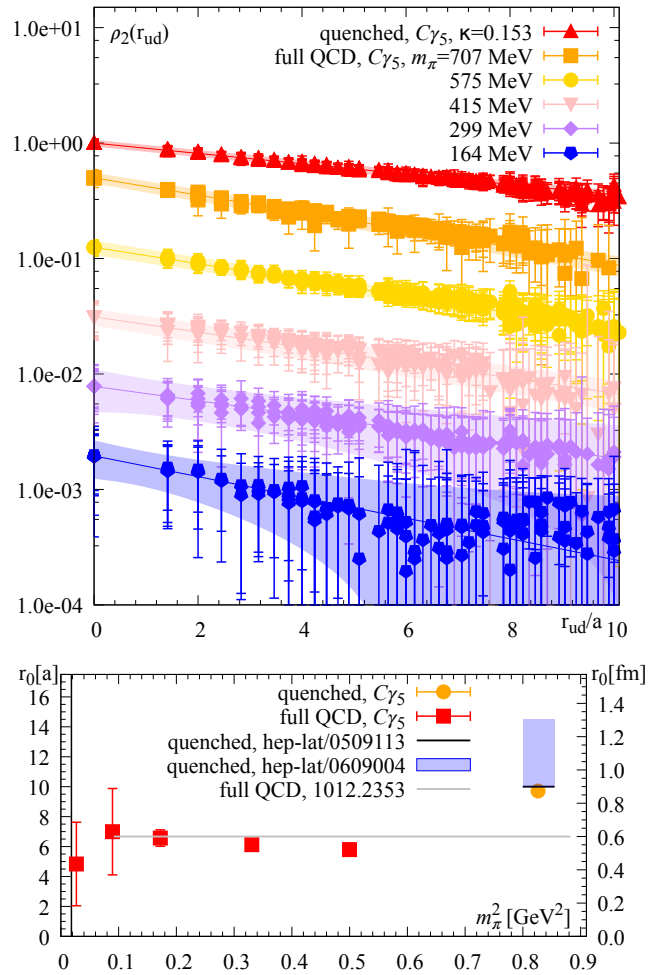


FIG. 4. Good diquark size. (Top) Exponential decay with  $r_{qq'}$  of the density-density correlator  $\rho_2^\perp(R, \Theta)$ . Each  $m_\pi$  has its own color. Data sets have been normalised at  $r_{qq'} = 0$  and offset vertically. Results for all available  $R$  are shown together in one colored set. Each colored band comes from the combined fit used to determine the diquark size  $r_0(m_\pi^2)$ . (Bottom) Resulting good diquark size  $r_0$  versus  $m_\pi^2$ , compared to results from the literature. The vertical line denotes physical  $m_\pi$ .

$r_0^\perp / r_0^\parallel(m_\pi^2) \simeq 1$  within errors for all  $m_\pi$ , indicating that the diquarks have a near-spherical shape. This is consistent with the scalar,  $J = 0$  nature of the good diquark, though the presence of the static quark could, in principle, have induced a diquark polarization. We conclude that there is no need to include a dipole term in diquark models.

*Summary and conclusions.*— Using a gauge-invariant setup, we have studied the masses and shapes of diquarks carrying different quantum numbers. Our study is the first to consider  $n_f = 2 + 1$  flavors of dynamical quarks with a range of  $u, d$  masses corresponding to  $m_\pi$  as low as 164 MeV. This allows for a small, controlled extrapolation to physical  $m_\pi \approx 135$  MeV. The resulting diquark mass differences presented in Fig. 1 and Tab. I confirm the special status of the “good” diquark channel, which shows an attraction of 198(4) MeV over the “bad” chan-

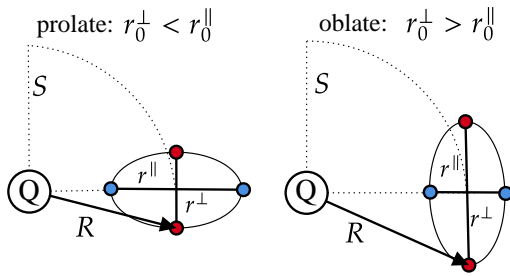


FIG. 5. *Diquark shape: 2D sketch of the 2 current insertions. Comparing exponential fall-offs in the  $\perp$  and  $\parallel$  directions gives a measure of the diquark shape: prolate (left) or oblate (right).*

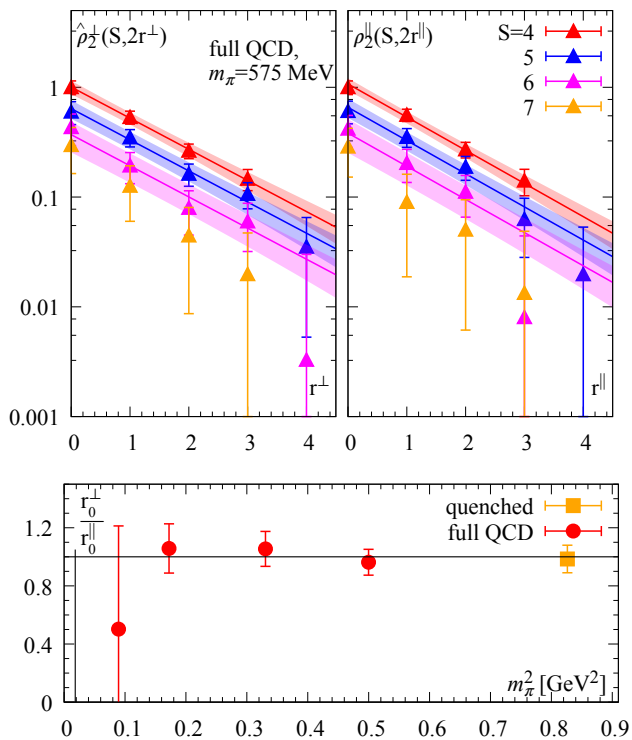


FIG. 6. *Good diquark shape. (Top)  $m_\pi = 575$  MeV results for the  $r_{qq'}$ -dependence of  $\rho_2(r_{qq'}, S, \phi)$  for tangential ( $\phi = \pi/2$ , left panel) and radial ( $\phi = \pi$ , right panel) quark-quark orientations. The colored error bands are the results of combined fits to data for each of  $S = 4a, 5a, 6a$  and  $7a$ . (Bottom) The ratio  $r_0^\perp/r_0^\parallel$  for all  $m_\pi$  considered here. The vertical line denotes physical  $m_\pi$ .*

nel, more over the others. A simple interpolation ansatz Eq. (2) accurately describes how this attraction varies with  $m_\pi$ , and with the diquark flavor composition. Extrapolation of our results to the continuum limit is still required, but this has been found to amount to a small correction, at the percent level, in other hadronic mass measurements on the same gauge configurations [28, 36, 37]. We have also measured the mass difference between a good diquark and an [anti]quark, as per Tab. I. The information obtained above may prove useful, both in iden-

tifying channels favorable to the existence of low-lying tetraquark or pentaquark states, and in obtaining rough estimates of their expected masses. Outstanding issues still to be investigated are potential distortions of the good diquark correlation caused by the presence of additional light quarks and/or the impact of Pauli blocking in channels where more than one good light diquark may be present.

In a second set of measurements, we have shown that the  $q - q$  attraction responsible for the bad-good diquark mass differences induces a compact spatial correlation, present in the “good” diquark channel only. The associated “good” diquark size, extracted from the spatial decay rate of quark density-density correlations, is  $\mathcal{O}(0.6)$  fm, similar to that of ordinary mesons and baryons [35], and varies little with the light-quark mass.

Finally, we have tried to refine the diquark picture further, by studying the shape - prolate or oblate - of quark density-density correlations in a good diquark, in the background of a heavy, static quark. It turns out that good diquarks are nearly spherical, with no signal within errors of a departure from this simplest shape.

Our three sets of results - bad-good diquark mass difference, good diquark size and shape - paint a diquark picture entirely consistent with that used in diquark models and provide clear, quantitative support for the good diquark picture. Diquark models are playing an important role in explorations of possible multi-quark exotics, especially in channels too complex to permit a complete theoretical analysis. In such channels, various light quark pairings into compact good diquark composites are likely to occur, especially when heavy  $c, b$  quark sources are present (see *e.g.* [38–40] for phenomenological and [30, 31, 41–51] for lattice studies). Which pairing is energetically favored depends sensitively on the numerical values of the parameters of the diquark model. Our study may sharpen these values, and help improve the reliability of such diquark analyses.

*Acknowledgements.* - Calculations were performed on the HPC clusters HPC-QCD@CERN and Niagara@SciNet supported by Compute Canada. AF thanks M. Bruno, B. Colquhoun, P. Fritzsche, J. Green and M. Hansen for discussions. PdF thanks R. Fukuda for his help with an earlier, not completed version of this project [26], and K. Fukushima for discussions. RL and KM acknowledge the support of grants from the Natural Sciences and Engineering Research Council of Canada. Together we thank R. J. Hudspith for reviewing an initial version of this manuscript.

- [1] M. Gell-Mann, Phys. Lett. **8**, 214 (1964).
- [2] M. Ida and R. Kobayashi, Prog. Theor. Phys. **36**, 846 (1966).
- [3] D. B. Lichtenberg, W. Namgung, E. Predazzi, and J. G. Wills, Phys. Rev. Lett. **48**, 1653 (1982).
- [4] R. Jaffe, Phys. Rept. **409**, 1 (2005), arXiv:hep-ph/0409065.
- [5] A. Ali, J. S. Lange, and S. Stone, Prog. Part. Nucl. Phys. **97**, 123 (2017), arXiv:1706.00610 [hep-ph].
- [6] M. Barabanov *et al.*, (2020), arXiv:2008.07630 [hep-ph].
- [7] R. T. Cahill, C. D. Roberts, and J. Praschifka, Phys. Rev. **D36**, 2804 (1987).
- [8] P. Maris, Few Body Syst. **32**, 41 (2002), arXiv:nucl-th/0204020 [nucl-th].
- [9] E. Santopinto, Phys. Rev. **C72**, 022201 (2005), arXiv:hep-ph/0412319 [hep-ph].
- [10] A. De Rujula, H. Georgi, and S. L. Glashow, Phys. Rev. **D12**, 147 (1975).
- [11] T. A. DeGrand, R. L. Jaffe, K. Johnson, and J. E. Kiskis, Phys. Rev. **D12**, 2060 (1975).
- [12] G. 't Hooft, Phys. Rev. **D14**, 3432 (1976), [Erratum: Phys. Rev. **D18**, 2199 (1978)].
- [13] E. V. Shuryak, Nucl. Phys. **B203**, 93 (1982).
- [14] T. Schäfer and E. V. Shuryak, Rev. Mod. Phys. **70**, 323 (1998), arXiv:hep-ph/9610451 [hep-ph].
- [15] M. Hess, F. Karsch, E. Laermann, and I. Wetzorke, Phys. Rev. **D58**, 111502 (1998), arXiv:hep-lat/9804023 [hep-lat].
- [16] Y. Bi, H. Cai, Y. Chen, M. Gong, Z. Liu, H.-X. Qiao, and Y.-B. Yang, Chin. Phys. C **40**, 073106 (2016), arXiv:1510.07354 [hep-ph].
- [17] R. Babich, N. Garron, C. Hoelbling, J. Howard, L. Lelouch, and C. Rebbi, Phys. Rev. **D76**, 074021 (2007), arXiv:hep-lat/0701023 [HEP-LAT].
- [18] K. B. Teo and J. W. Negele, *LATTICE 93: 11th International Symposium on Lattice Field Theory Dallas, Texas, October 12-16, 1993*, Nucl. Phys. Proc. Suppl. **34**, 390 (1994).
- [19] J. W. Negele, in *Excited nucleons and hadronic structure. Proceedings, Conference, NSTAR 2000, Newport News, USA, February 16-19, 2000* (2000) pp. 368–377, arXiv:hep-lat/0007026 [hep-lat].
- [20] C. Alexandrou, P. de Forcrand, and A. Tsapalis, Phys. Rev. **D66**, 094503 (2002), arXiv:hep-lat/0206026 [hep-lat].
- [21] K. Orginos, PoS **LAT2005**, 054 (2006), arXiv:hep-lat/0510082.
- [22] C. Alexandrou, P. de Forcrand, and B. Lucini, PoS **LAT2005**, 053 (2006), arXiv:hep-lat/0509113.
- [23] C. Alexandrou, P. de Forcrand, and B. Lucini, Phys. Rev. Lett. **97**, 222002 (2006), arXiv:hep-lat/0609004.
- [24] J. Green, J. Negele, M. Engelhardt, and P. Varilly, PoS **LATTICE2010**, 140 (2010), arXiv:1012.2353 [hep-lat].
- [25] J. Green, M. Engelhardt, J. Negele, and P. Varilly, AIP Conf. Proc. **1441**, 172 (2012).
- [26] R. Fukuda and P. de Forcrand, PoS **LATTICE2016**, 121 (2017).
- [27] S. Aoki *et al.* (PACS-CS), Phys. Rev. D **79**, 034503 (2009), arXiv:0807.1661 [hep-lat].
- [28] Y. Namekawa *et al.* (PACS-CS), Phys. Rev. D **87**, 094512 (2013), arXiv:1301.4743 [hep-lat].
- [29] <https://www.jldg.org>.
- [30] A. Francis, R. J. Hudspith, R. Lewis, and K. Maltman, Phys. Rev. Lett. **118**, 142001 (2017), arXiv:1607.05214 [hep-lat].
- [31] A. Francis, R. J. Hudspith, R. Lewis, and K. Maltman, Phys. Rev. D **99**, 054505 (2019), arXiv:1810.10550 [hep-lat].
- [32] M. Della Morte, A. Shindler, and R. Sommer, JHEP **08**, 051 (2005), arXiv:hep-lat/0506008.
- [33] M. Donnellan, F. Knechtli, B. Leder, and R. Sommer, Nucl. Phys. B **849**, 45 (2011), arXiv:1012.3037 [hep-lat].
- [34] The slight difference in the two  $0^+$  results originates from their two different renormalisation constants. Unfortunately these are not available for the ensembles studied.
- [35] B. Blossier and A. Gérardin, Phys. Rev. D **94**, 074504 (2016), arXiv:1604.02891 [hep-lat].
- [36] M. Padmanath, (2019), arXiv:1905.10168 [hep-lat].
- [37] R. J. Hudspith, A. Francis, R. Lewis, and K. Maltman, PoS **LATTICE2016**, 133 (2017).
- [38] M. Karliner and J. L. Rosner, Phys. Rev. Lett. **119**, 202001 (2017), arXiv:1707.07666 [hep-ph].
- [39] E. J. Eichten and C. Quigg, Phys. Rev. Lett. **119**, 202002 (2017), arXiv:1707.09575 [hep-ph].
- [40] A. Czarnecki, B. Leng, and M. B. Voloshin, Phys. Lett. B **778**, 233 (2018), arXiv:1708.04594 [hep-ph].
- [41] M. Wagner (ETM), Acta Phys. Polon. Supp. **4**, 747 (2011), arXiv:1103.5147 [hep-lat].
- [42] Z. S. Brown and K. Orginos, Phys. Rev. D **86**, 114506 (2012), arXiv:1210.1953 [hep-lat].
- [43] P. Bicudo, K. Cichy, A. Peters, and M. Wagner, Phys. Rev. D **93**, 034501 (2016), arXiv:1510.03441 [hep-lat].
- [44] P. Bicudo and M. Wagner (European Twisted Mass), Phys. Rev. D **87**, 114511 (2013), arXiv:1209.6274 [hep-ph].
- [45] P. Bicudo, K. Cichy, A. Peters, B. Wagenbach, and M. Wagner, Phys. Rev. D **92**, 014507 (2015), arXiv:1505.00613 [hep-lat].
- [46] P. Bicudo, J. Scheumert, and M. Wagner, Phys. Rev. D **95**, 034502 (2017), arXiv:1612.02758 [hep-lat].
- [47] P. Junnarkar, N. Mathur, and M. Padmanath, Phys. Rev. D **99**, 034507 (2019), arXiv:1810.12285 [hep-lat].
- [48] L. Leskovec, S. Meinel, M. Pflaumer, and M. Wagner, Phys. Rev. D **100**, 014503 (2019), arXiv:1904.04197 [hep-lat].
- [49] R. J. Hudspith, B. Colquhoun, A. Francis, R. Lewis, and K. Maltman, Phys. Rev. D **102**, 114506 (2020), arXiv:2006.14294 [hep-lat].
- [50] P. Mohanta and S. Basak, Phys. Rev. D **102**, 094516 (2020), arXiv:2008.11146 [hep-lat].
- [51] P. Bicudo, A. Peters, S. Velten, and M. Wagner, (2021), arXiv:2101.00723 [hep-lat].
- [52] P. A. Zyla *et al.* (Particle Data Group), PTEP **2020**, 083C01 (2020).
- [53] A. Francis, R. J. Hudspith, R. Lewis, and K. Maltman, PoS **LATTICE2016**, 132 (2016).
- [54] <http://luscher.web.cern.ch/luscher/DD-HMC/>.
- [55] R. Hudspith (RBC, UKQCD), Comput. Phys. Commun. **187**, 115 (2015), arXiv:1405.5812 [hep-lat].
- [56] <https://github.com/RJHudspith/GLU/>.
- [57] A. Hasenfratz and F. Knechtli, Phys. Rev. D **64**, 034504 (2001), arXiv:hep-lat/0103029.

# Supplemental Materials: Diquark properties from full QCD lattice simulations

## I. PHENOMENOLOGICAL EXPECTATIONS

Phenomenological estimates for the static-limit values of the bad-good diquark and diquark-antiquark mass differences were discussed in detail in Ref. [4]. These are most reliably obtained using experimental results for combinations of charm and bottom hadron masses for which leading  $O(1/m_Q)$  ( $Q = c, b$ ) contributions vanish.

Ref. [4] gives expressions for the combinations needed to provide phenomenological estimates for four of the splittings we have measured. Explicitly, the combination

$$\frac{1}{3}(2M(\Sigma_Q^*) + M(\Sigma_Q)) - M(\Lambda_Q) \quad (\text{S1})$$

provides an estimate for  $\delta(1^+ - 0^+)_{ud}$ , the combination

$$\frac{2}{3}(M(\Xi_Q^*) + M(\Sigma_Q) + M(\Omega_Q)) - M(\Xi_Q) - M(\Xi_Q')$$

(S2)

an estimate for  $\delta(1^+ - 0^+)_{us}$ , the combination

$$M(\Lambda_Q) - \frac{1}{4}(M(P_{Qu}) + 3M(V_{Qu})), \quad (\text{S3})$$

with  $P_{Qu}$  and  $V_{Qu}$  the ground-state, heavy-light pseudoscalar and vector mesons, an estimate for  $\delta(Q[ud]_{0^+} - \bar{Q}u)$ , and the combination

$$M(\Xi_Q) + M(\Xi_Q') - \frac{1}{2}(M(\Sigma_Q) + M(\Omega_Q)) - \frac{1}{4}(M(P_{Qs}) + 3M(V_{Qs})), \quad (\text{S4})$$

with  $P_{Qs}$  and  $V_{Qs}$  the ground-state, heavy-strange pseudoscalar and vector mesons, an estimate for  $\delta(Q[us]_{0^+} - \bar{Q}s)$ . For a given static-limit splitting, the most accurate estimate should be that obtained using bottom hadron input, while the difference between the charm- and bottom-based estimates should provide a conservative assessment of the deviation of the bottom-based estimate from the actual static-limit value. At the time Ref. [4] was written, information on bottom hadron masses was limited, and only one of these four splittings,  $\delta(Q[ud]_{0^+} - \bar{Q}u)$ , could be estimated with both charm and bottom input. The agreement between the two was excellent. It is now possible to estimate all four splittings using both charm and bottom input. Using PDG 2021 input [52], we find, for  $\delta(1^+ - 0^+)_{ud}$ , 210 MeV using charm input and 206 MeV using bottom input; for  $\delta(1^+ - 0^+)_{us}$ , 148 MeV using charm input and 145 MeV using bottom input; for  $\delta(Q[ud]_{0^+} - \bar{Q}u)$ , 313 MeV using charm input and 306 MeV using bottom input; and, for  $\delta(Q[us]_{0^+} - \bar{Q}s)$  398 MeV using charm input and 397 MeV using bottom input. It follows that the bottom-based phenomenological estimates for the static-limit splittings should be reliable to  $O(7)$  MeV or better. These estimates agree well with the results shown in Tab. I.

## II. LATTICE ENSEMBLES AND PROPAGATORS

For the numerical studies, we re-use the set of propagators from [30, 31] determined on the publicly available  $n_f = 2 + 1$  flavor full QCD gauge ensembles provided by the PACS-CS'09 collaboration [27, 28] via the JLDG repository [29]. The quoted values of  $m_\pi$  and lattice spacing originate from our own previous re-determination [37, 53]. These gauge configurations have been used extensively within the lattice community. A known caveat is the slight mistuning of the strange sea quark mass [27]. The value of the hopping parameter which produces the physical strange quark mass is, however, known, and we set the strange valence quark mass to this value, thus introducing a tiny amount of partial quenching.

To connect with previous studies in the quenched setup discussed in [23], and in more detail in [22], we generated a new ensemble with the same lattice parameters, in particular with coupling  $\beta = 6.0$  and hopping parameter  $\kappa = 0.153$  for propagator inversions. This corresponds to a valence pion mass  $m_\pi^v = 909$  MeV.

All propagators were computed using the deflated SAP-GCR solver [54] and have Coulomb gauge-fixed wall sources, where the gauge was fixed using the FACG algorithm in the implementation of [55, 56].

We can re-use the propagators without further inversions since the gauge-fixed wall sources enable the contraction of the density correlators without an additional sequential source propagator. Choosing  $(t_{snk} - t_{src}) = 16$  enables us to perform multiple measurements on each configuration. Setting  $t_m$  midway between source and sink minimizes excited-state contamination.

For the static quark we compute propagators on the fly via  $(t_2 > t_1)$ [32]:

$$S(\mathbf{x}, t_2, \mathbf{x}, t_1) = \left(\frac{1 + \gamma_0}{2}\right) \left[ \prod_{t=t_1}^{t_2-a} U_0(\mathbf{x}, t) \right] \quad (\text{S5})$$

where we dropped the exponential prefactor, since it amounts to a constant shift in the masses that either drops out in the difference or is irrelevant to the results. To reduce statistical fluctuations, the gauge links are smeared using HYP smearing (type 1 [33, 57]) in all 4 dimensions, which introduces some non-locality in time. In all cases we made sure that the propagation time  $t$  is large enough and the number of smearing steps small enough to ensure negligible effects aside from the boosted signal. Furthermore we considered several smearing setups and smearing radii. We observed comparable results and selected the one giving the best signal-to-noise properties. Our lattice parameters are listed in Tab. S1.

Label	$L \times T$	$a^{-1}$ [GeV]	$m_\pi$ [MeV]	$n_{cfg}$	$n_{meas}^{spec}$	$n_{meas}^{struct}$
Q	$32 \times 64$	2.15	909	374	374	374
E1	$32 \times 64$	2.194	707	399	1596	798
E2	"	"	575	400	1600	800
E4	"	"	415	400	3200	2800
E5	"	"	299	800	6400	5600
E6	"	"	164	198	6336	2574

TABLE S1. Parameters of the lattice calculation.  $n_{meas}^{spec}$  and  $n_{meas}^{struct}$  indicate how many measurements in total were made of the baryon/meson correlators for the spectroscopy study, and of the density-density correlators for the structure analysis, respectively. For the latter analysis, the sink-source time propagation is set to  $(t_{snk} - t_{src}) = 16$ , with the currents inserted at  $t_m = 8$ , see also the sketch in Fig. 2.

### III. LATTICE SPECTROSCOPY ANALYSIS DETAILS

To study the mass differences between good and bad diquarks, shown in Fig. 1 (top left and top right), we fix the energies in the following way: First, we analyze the smeared and unsmeared correlators separately. For each dataset, we consider one- and two-state fits. The fit window in Euclidean time is the longest for which both fits give ground state energies consistent within errors. The ground state energies of the smeared and unsmeared data sets are then averaged, and the larger of the two uncertainties assigned as the final error.

When performing the extrapolations to physical  $m_\pi$ , we also considered combined fits with the Ansatz Eq. (2) using free  $n$  and shared  $B$ , but did not find an improvement and therefore quote results from individual fits. As a further consistency check note that all three extrapolations intersect for large  $m_\pi$  at the  $n_f = 3$  flavor-symmetric point without having enforced this expectation through a shared parameter.

In Fig. 1 (bottom left) we show the difference in mass between single-static octet baryons and static-light pseudoscalar mesons, as explained in the text. In this data the excited state contamination is much larger and we extract the masses by fitting both smeared and unsmeared data with a two-state Ansatz. As before we take the values from the longest time interval where the fitted ground states agree within errors, average the results, and quote the larger of the two uncertainties as our error. For the  $ud - u$ ,  $ls - s$  and  $ls - l$  cases we observe the expected  $n_f = 3$  degeneracy as  $m_{u,d} \rightarrow m_s$ .

In Fig. 1 (bottom right) we show the comparison of the bad-good diquark mass difference, multiplied by the expected factor  $3/2$ , and the corresponding  $\Delta - N$  mass splitting. Measurements of the latter were newly performed for this study, using the same propagators as for the static baryons shown so far. Since in this case we do not benefit from the cancellation of the heavy quark mass, and nucleon correlators generally suffer from the well known signal-to-noise problem, we expect larger uncertainties in this study. The situation is further com-

plicated as the  $\Delta$  baryon is a resonance in nature: a single operator analysis, as performed here, can capture only its rough features. To stabilise the extraction of the masses here, we fitted the channel pairs  $\Gamma = (\gamma_i, \sigma_{i0})$  and  $(\gamma_5, \gamma_5 \gamma_0)$  simultaneously with single exponentials and chose to quote the parameters from the longest combined plateau. For the physical-point extrapolation, the results were fitted to the same Ansatz Eq. (2), in the same way as before.

### IV. LATTICE STRUCTURE ANALYSIS DETAILS

The diquark size  $r_0$  can be estimated from the fitted rate of the exponential decay,  $\sim \exp(-r_{qq'}/r_0)$  of the density-density correlator  $\rho_2^\perp(R, r_{qq'})$ , with  $r_{qq'}$  the distance between the two current insertion points: see Fig. 4 (top).

The colored bands (one for each  $m_\pi$ ) are the result of performing a combined fit for all available  $R$  to a single exponential with shared size parameter  $r_0$  and separate amplitudes. Note that our lattice spatial size is about  $5r_0$ , so we neglect corrections caused by periodic boundary conditions which were studied in [24]. We checked the dependence of  $r_0(R)$  on  $R$  through individual fits and found no significant dependence for  $R \in [3 : 6]$ . Similar findings were reported in [22]. Of course, if  $R$  is increased beyond  $\sim 1$  fm, the effective string between the static quark and the diquark will break and a light baryon will form, with qualitatively different diquark correlations. Our study does not consider this large-distance regime. Also, for a given  $R$ , we normally would quote the number from the largest stable fit window. However, due to our chosen geometry we may expect interference from the static quark when  $r_{qq'} \gtrsim R$ , and we limit the fit window accordingly.

Separate sizes  $r_0^\perp$  and  $r_0^\parallel$  can be defined for the tangential and radial geometries shown in Fig. 5. The ratio of sizes  $r_0^\perp/r_0^\parallel$  then gives a measure of whether the diquarks are spherical ( $r_0^\perp/r_0^\parallel = 1$ ), prolate ( $r_0^\perp/r_0^\parallel < 1$ ), or oblate ( $r_0^\perp/r_0^\parallel > 1$ ).

To estimate  $r_0^\perp$  and  $r_0^\parallel$ , we measure  $\rho_2(r_{qq'}, S, \phi)$  for the two geometries of Fig. 5, with  $r_0^\perp$  and  $r_0^\parallel$  corresponding to  $\phi = \pi/2$  and  $\pi$  in Fig. 2, respectively. When the line labelled  $S$  in Fig. 2 points along the  $x$  axis, the current insertion points for the radial configuration (the blue points in Fig. 5) are  $x_{1,2} = (S \pm r^\parallel, 0, 0)$ , while those for the tangential configuration (the red points in Fig. 5) are  $x_{1,2} = (S, \pm r^\perp, 0)$ . For simplicity, we take the line labelled  $S$  to always lie in one of the  $x$ ,  $y$  or  $z$  axis directions, considering all such permutations.

Focusing first on the radial case,  $x_1 + x_2 = 2S$  is constant at fixed  $S$  and independent of  $r^\parallel$ . Here we define our radial size parameter,  $r_0^\parallel$ , at this fixed  $S$ , by fitting

the  $r^{\parallel}$  dependence to the form

$$\rho_2^{\parallel}(S, r^{\parallel}) \sim \exp(-r^{\parallel}/r_0^{\parallel}) . \quad (\text{S6})$$

Since no obvious  $S$  dependence is observed, we arrive at  $r_0^{\parallel}$  by analyzing the data in a combined fit for several  $S$  using the same fit method applied before.

In the tangential case, a complication arises. Our previously introduced size parameter,  $r_0$ , was defined through a fit to  $\rho_2^{\perp}(R, r^{\perp})$  with variable  $r^{\perp}$ , but fixed  $R$ . Since, however,  $R = \sqrt{(r^{\perp})^2 + S^2}$ , when  $r^{\perp}$  varies at fixed  $R$ ,  $S$  also varies. This is not the fixed- $S$  situation used to define  $r_0^{\parallel}$ . We thus need to define an alternate tangential size parameter,  $r_0^{\perp}$ , through a fit to data with variable  $r^{\perp}$  but fixed  $S$ , in order to compare tangential and radial size parameters both defined at fixed  $S$ . As seen above, the density-density correlation  $\rho_2^{\perp}(R, r^{\perp})$  at fixed  $r^{\perp}$  varies with  $R$ . We find this dependence well described by an exponential form  $\sim \exp(-2R/R_0)$ . The dependence of the density-density correlation on  $r^{\perp}$  at fixed  $S$  in the tangential configuration can then be obtained by fitting the product  $\rho_2^{\perp}(R, r^{\perp}) \exp(+2R/R_0)$ , evaluated at fixed  $S$  and variable  $r^{\perp}$ , to the form  $\exp(-r^{\perp}/r_0^{\perp})$ . Since the fixed- $S$  tangential  $r^{\perp} = 0$  and radial  $r^{\parallel} = 0$  configurations are geometrically degenerate, it is convenient to instead use the form  $\exp(-r^{\perp}/r_0^{\perp})$  to fit the modified product

$$\hat{\rho}_2^{\perp}(S, 2r^{\perp}) = \rho_2(R, 2r^{\perp}) \exp\left(+\frac{2R}{R_0}\right) \exp\left(-\frac{2S}{R_0}\right), \quad (\text{S7})$$

with  $R_0$  a second fit parameter, and the right-hand side evaluated at fixed  $S$ . The extra  $r^{\perp}$ -independent factor,  $\exp(-2S/R_0)$ , ensures that, in the limit that  $r^{\perp} \rightarrow 0$  and hence  $R \rightarrow S$ , the quantity being fit reduces to

$\rho_2^{\perp}(R = S, r^{\perp} = 0)$ . Since this is identical to the analogous zero-separation quantity,  $\rho_2^{\parallel}(S, r^{\parallel} = 0)$ , which enters the fit used to determine  $r_0^{\parallel}$ , this choice ensures a common normalization for the tangential and radial fits, at the  $r^{\perp} = r^{\parallel} = 0$  point common to both.

In the top left and top right panels of Fig. 6 we show, for the  $m_{\pi} = 575$  MeV ensemble and  $S$  ranging from 4 to 7 times the lattice spacing, the dependences of  $\hat{\rho}_2^{\perp}(S, 2r^{\perp})$  on  $r^{\perp}$  and  $\rho_2^{\parallel}(S, 2r^{\parallel})$  on  $r^{\parallel}$ , respectively. Note that, in contrast to the presentation in Fig. 4 (top), results for different  $m_{\pi}$  have not been normalized at zero separation and offset vertically. Instead  $\hat{\rho}_2^{\perp}(S, 2r^{\perp})$  and  $\rho_2^{\parallel}(S, 2r^{\parallel})$  have been normalized to 1 at  $S = 4a$  and zero separation.

While the parameters  $r_0^{\perp}$  and  $R_0$  have been determined in the two-parameter fit described above,  $R_0$  could, in principle, also be determined by fitting  $\rho_2^{\perp}(R, r^{\perp})$ , with  $r^{\perp}$  fixed to zero, to the form  $\sim \exp(-2R/R_0)$ .

We found that inserting the resulting  $R_0$  into the Ansatz Eq. (S7) and subsequently fitting  $r_0^{\perp}$  produced no improvement over the direct two-parameter fit result, once errors were propagated and correlations taken into account.

In both the radial and tangential cases, we have propagated all errors within a bootstrap procedure, which allows us to also evaluate the uncertainty on the ratio  $r_0^{\perp}/r_0^{\parallel}$  consistently. Results for this ratio are shown as a function of  $m_{\pi}^2$  in the bottom panel of Fig. 6. We observe that the errors on the data limit the precision of the analysis, with a stable result, for example, not even attainable for the  $m_{\pi} = 164$  MeV ensemble. This is due in part to the noisiness of the results at large  $S$ , which were not precise enough to constrain  $R_0$ ,  $r_0^{\perp}$  and  $r_0^{\parallel}$  further.